



Distinct Fe K Line Complexes in MAXIJ1744–294 Revealed by XRISM High-resolution Spectroscopy

Kaushik Chatterjee^{1,2}, Santanu Mondal³, Biswaraj Palit⁴, Chandra B. Singh^{1,2}, Sujoy Kumar Nath⁵, Mayukh Pahari⁶, Brajesh Kumar^{1,2}, Wei Wang⁷, Hsiang-Kuang Chang⁸, and Xiaowei Liu^{1,2}

¹ South-Western Institute for Astronomy Research (SWIFAR), Yunnan University, Kunming, Yunnan 650500, People's Republic of China; mails.kc.physics@gmail.com, kaushik@ynu.edu.cn

² Key Laboratory of Survey Science of Yunnan Province, Yunnan University, Kunming, Yunnan 650500, People's Republic of China

³ Indian Institute of Astrophysics, II Block, Koramangala, Bengaluru 560034, Karnataka, India; santanuicsp@gmail.com

⁴ Nicolaus Copernicus Astronomical Center, Polish Academy of Sciences, ul. Bartycka 18, 00-716 Warsaw, Poland; bpalit@camk.edu.pl

⁵ Indian Center for Space Physics, 466 Barakhola, Netaji Nagar, Kolkata 700099, India

⁶ Department of Physics, Indian Institute of Technology Hyderabad, Hyderabad, Kandi, 502285 Sangareddy, India

⁷ Department of Astronomy, School of Physics and Technology, Wuhan University, Wuhan, People's Republic of China

⁸ Institute of Astronomy, National Tsing Hua University, Hsinchu 300044, Taiwan, People's Republic of China

Received 2025 June 30; revised 2025 August 18; accepted 2025 September 15; published 2025 October 17

Abstract

The newly discovered Galactic transient MAXIJ1744–294 went into its first X-ray outburst in 2025. We study the spectral properties of this source in the 2–10 keV energy band during this outburst using X-ray data from the XRISM satellite for both of its Resolve and Xtend instruments, taken on 2025 March 3. High-resolution spectroscopy has revealed, for the first time, complex iron line features in this source, corresponding to distinct components of Fe XXV emission and Fe XXVI absorption lines. Such a detailed structure has not been reported in other low-mass X-ray binaries to date, prior to the XRISM era. Our analysis shows that the line complexes arise from two highly ionized plasmas with an ionization rate $\sim 10^3 \text{ erg cm s}^{-1}$ with distinct turbulent velocities—one broad ($v_{\text{turb}} \approx 2513 \text{ km s}^{-1}$) from hot gas at the inner accretion disk and one narrow ($v_{\text{turb}} \approx 153 \text{ km s}^{-1}$) scattered by nearby photoionized gas. These results offer new insight into the reprocessing of continuum in stratified media, either in the accretion disk or winds, or both, for X-ray binaries in the soft state. The data are well described by models with spin, mass of the black hole, and accretion disk inclination $0.63\text{--}0.70$, $7.9 \pm 2.2 M_{\odot}$, and $19^{\circ}\text{--}24^{\circ}$. The fitted spectral model parameters suggest that the source is in the soft spectral state. The source is situated in a crowded field near the Galactic center, resulting in a large hydrogen column density.

Unified Astronomy Thesaurus concepts: Black holes (162); Compact radiation sources (289); X-ray binary stars (1811); Stellar accretion disks (1579)

1. Introduction

Transient compact objects show variability signatures in the spectral and temporal properties during their outburst phases. These properties are strongly correlated with each other across different spectral states (R. A. Remillard & J. E. McClintock 2006; S. K. Chakrabarti et al. 2008; B. E. Tetarenko et al. 2016, and references therein). In different spectral states, the appearance and disappearance of timing phenomena like quasiperiodic oscillations, or QPOs, have been observed (e.g., T. Belloni et al. 2002; P. Casella et al. 2005; S. Motta et al. 2011; S. Mondal et al. 2014; K. Chatterjee et al. 2020, 2024, 2025, and references therein). Additionally, jets or outflows are often observed phenomena that leave imprints in different spectral states (R. A. Sunyaev & L. G. Titarchuk 1980; S. K. Chakrabarti 1999; V. Dhawan et al. 2000; S. Corbel & R. P. Fender 2002; S. Mondal & S. K. Chakrabarti 2021). Therefore, their X-ray spectra can tell us the underlying physical processes responsible for the spectral features.

The observed spectral features mainly come from two distinct regions: one is the inner hot puffed-up region, or so-called corona, and the second component is the cold Keplerian disk. The seed photons from the cold disk produce the

blackbody spectrum, and some fraction of these photons is upscattered by the corona and gives rise to the hard X-ray radiation (R. A. Sunyaev & L. G. Titarchuk 1980; F. Haardt & L. Maraschi 1993; S. Chakrabarti & L. G. Titarchuk 1995; C. Done et al. 2007, and references therein). Some of the hard photons from the corona fall back to the disk and come out as the so-called reflection component (I. M. George & A. C. Fabian 1991; R. R. Ross & A. C. Fabian 2005) leaving a hump above 10 keV (R. R. Ross & A. C. Fabian 2005; J. García & T. R. Kallman 2010), which is believed to be the origin of the Fe K fluorescent line around 6.4 keV (L. A. Pozdnyakov et al. 1983; A. C. Fabian et al. 1989). However, the origin of the hump above 10 keV can also be from the radiation coming from the bulk motion Comptonization effect in the jet (L. Titarchuk & C. Shrader 2005; S. Mondal & S. K. Chakrabarti 2021). All these components of the radiation are informative in understanding the accretion behavior near the black hole (BH) due to the strong gravitational effect, reflected in the Fe $K\alpha$ line profile (L. W. Brenneman & C. S. Reynolds 2006; A. Marinucci et al. 2014). The line can break into a double horn if the accretion disk moves much closer to the BH (A. C. Fabian et al. 1989; K. Iwasawa et al. 1996, and references therein), helping to estimate the spin of the central BH (L.-X. Li et al. 2005; S. Mondal et al. 2024, and references therein).

Apart from the Fe $K\alpha$ line, there may be the presence of other Fe line components also in the 6.3–7.3 keV energy band.



Original content from this work may be used under the terms of the [Creative Commons Attribution 4.0 licence](https://creativecommons.org/licenses/by/4.0/). Any further distribution of this work must maintain attribution to the author(s) and the title of the work, journal citation and DOI.

Multiple iron line emissions can be observed, which might be associated with the Galactic diffuse X-ray emission, or it can also be due to the physical conditions of the accreting matter (see S. Mondal et al. 2021 for numerical simulations). The ~ 6.6 – 6.7 keV iron line emission plays a significant role in the context of our Galaxy. The emission line at ~ 6.6 – 6.7 keV can be identified as a combination of the 6.63, 6.67, and 6.70 keV lines of Fe XXV ions, which could be produced through the recombination process in the accretion disk corona (K. Asai et al. 2000). The measurements of these features require high-quality X-ray data. The spectacular resolution of the XRISM (M. Tashiro et al. 2021) data can reveal these multiple line peaks and their origin.

The new Galactic source MAXI J1744–294 was reported on 2025 January 2 (Y. Kudo et al. 2025; M. Nakajima et al. 2025; S. Watanabe et al. 2025) by the Monitor of All-sky X-ray Image or MAXI (M. Matsuoka et al. 2009) with a flux level of ~ 250 mCrab. From the follow-up observations of Swift/XRT, two sources were detected near Sgr A*, one of which is consistent with the position of the neutron star low-mass X-ray binary AX J1745.6–2901, while the other one is an uncatalogued target at coordinates 17:45:41.93, $-29:00:35$ in J2000 coordinates (C. O. Heinke et al. 2025). Later on 2025 February 6, NuSTAR also confirmed some activity from this new source (S. Mandel et al. 2025). It was observed on 2025 February 11–12, using NICER data by G. K. Jaisawal et al. (2025). They reported the presence of an absorbed power law along with a disk blackbody component in the 2–10 keV energy band with an iron line at 6.6 ± 0.9 keV. The authors reported a high column density of $N_H = (11 \pm 1) \times 10^{22} \text{ cm}^{-2}$. This source is located very close to the Galactic center with (R.A., decl.) = (266.116 deg, -29.433 deg). For the estimation of flux in the 2–10 keV, S. Mandel et al. (2025) assumed a distance of 8 kpc. Their estimated spectral parameters are consistent with those of a low-mass black hole X-ray binary in the soft state. Recently, S. Majumder et al. (2025) analyzed the IXPE data of the source and could not detect any polarization signature. Along the same line, L. Marra et al. (2025) found only a $\sim 1.3\%$ polarization degree using IXPE data and constrained the disk inclination angle of the source in a broad range of 38° – 71° . A possible cause may be due to the presence of the soft spectral state, where a significantly low or null detection is favorable for several reasons (see S. Mondal et al. 2024).

In this work, we have analyzed XRISM spectra for both the *Resolve* and *Xtend* instruments in the 2–10 keV energy band of the newly detected Galactic source MAXI J1744–294 during its recent outburst in 2025. We have implemented some phenomenological and physical models for this analysis. In the next section, we describe the data reduction procedure. In Section 3, we discuss the spectral analysis and results. Finally, we draw our conclusions in Section 4.

2. Data Reduction

We have used XRISM data from both instruments that observed the source on 2025 March 3 (MJD 60737; Obs ID 901002010) for this work. The data reduction procedure is discussed below.

The data of the new Galactic source MAXI J1744–294 is downloaded from the publicly available HEASARC archive.⁹

⁹ <https://heasarc.gsfc.nasa.gov/cgi-bin/W3Browse/w3browse.pl>

Although level-2 cleaned event files are already present in the downloaded data, we reprocessed the data using the `xapipeline` task for both the *Resolve* and *Xtend* instruments separately. After the production of the level-2 cleaned files, as recommended in the Quick-Start Guide Version 2.3,¹⁰ we used additional screening for pulse rise time, event type, and status. We also excluded the events from pixel number 27, as it is recommended for calibration uncertainties. We use the `XSELECT` task to extract spectra and light-curve files for science analysis. Then we use `rslmkrmf` and `xtdrmf` commands to make response files for the *Resolve* and *Xtend* instruments. We have used the extra-large (XL) type of response file for *Resolve*. Next, using the `xaexpmap` command, we create a standard exposure map for both instruments. Then, we create ancillary response files for both instruments using the `xaarfgen` command. We have also created the non-X-ray background for *Resolve* using the `rslnxbgen` command.

3. Spectral Analysis and Results

We perform spectral analysis of the newly detected Galactic source MAXI J1744–294 using the processed data for science results. We used `XSPEC`¹¹ (K. A. Arnaud 1996) to model the data using both phenomenological and physical models.¹² To account for the continuum emission, we have used combinations of models by using a disk blackbody,¹³ a `kerrbb`,¹⁴ and a power-law¹⁵ model. We have also used the two-component advective flow model (TCAF; S. Chakrabarti & L. G. Titarchuk 1995), including jet or `JeTCAF` (S. Mondal & S. K. Chakrabarti 2021) as part of the physical modeling. For the interstellar absorption, we have used the multiplicative absorption model component `tbabs`.¹⁶ Different combinations of these four models can fit the continuum satisfactorily. However, some line features are also present in the spectrum, particularly near the 6.3–7.3 keV energy band. Thus, we added multiple Gaussian¹⁷ lines to fit these lines. This model combination is applied to both instruments.

Furthermore, we have also performed photoionization modeling in the 5–8 keV energy band to study the distinct iron line emission complexes and their origin. We discuss all these results in broad detail in the following subsections.

3.1. Continuum Modeling

First, we looked at the spectra of *Resolve* in the 6.3–7.3 keV. This is shown in the upper panel of Figure 1. This shows that distinct multiple line features are present in the 6.3–7.3 keV energy band. There are line emission profiles in the *Resolve* spectrum, which might be related to the Fe XXV

¹⁰ https://heasarc.gsfc.nasa.gov/docs/xrism/analysis/quickstart/xrism_quick_start_guide_v2p3_240918a.pdf

¹¹ <https://heasarc.gsfc.nasa.gov/docs/software/xspec/>

¹² <https://heasarc.gsfc.nasa.gov/docs/software/xspec/manual/node129.html>

¹³ <https://heasarc.gsfc.nasa.gov/docs/software/xspec/manual/node165.html>

¹⁴ <https://heasarc.gsfc.nasa.gov/docs/software/xspec/manual/node189.html>

¹⁵ <https://heasarc.gsfc.nasa.gov/docs/software/xspec/manual/node221.html>

¹⁶ <https://heasarc.gsfc.nasa.gov/docs/software/xspec/manual/node279.html>

¹⁷ <https://heasarc.gsfc.nasa.gov/docs/software/xspec/manual/node181.html>

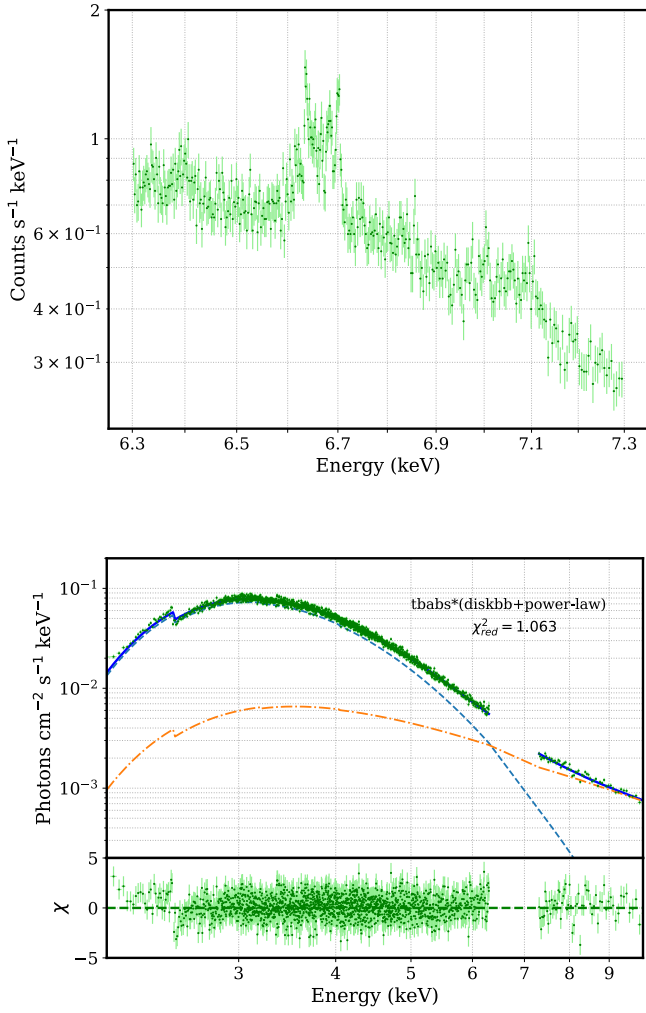


Figure 1. The Resolve spectrum in the range 6.3–7.3 keV is shown in the upper panel. The lower panel represents the fitted continuum in the 2–10 keV energy band, ignoring the 6.3–7.3 keV region.

line. That prompted us to first analyze the continuum spectrum and find a suitable model combination for the continuum emission. For that, we ignored the 6.3–7.3 keV energy region and fitted the data using the model combination `tbabs*(-diskbb + po)`. We found that the model best fits the continuum with $\chi^2_{\text{red}} = 1.06$, as shown in the lower panel of Figure 1.

Next, we looked at the Xtend spectrum and performed the same exercise. The upper panel of Figure 2 shows Fe line features in the spectrum from Xtend in the 6.3–7.3 keV energy band. Unlike the Resolve spectrum, this is not clearly resolved in the 6.3–7.3 keV energy band, whether there are multiple line features or not. However, both spectra can certainly show the presence of the Fe line profile in the energy range of 6.3–7.3 keV. Thus, we fit the continuum, excluding this energy band. For the Xtend spectrum, we found that the previous continuum model combination was not good enough. There is an excess of flux at ~ 2.4 keV, which could be an instrumental calibration effect rather than astrophysical. The $\chi^2_{\text{red}} = 4.284$. This can be noticed in the middle panel of Figure 2. By adding another Gaussian (*ga*) model, we achieve the best fit for the continuum. The model

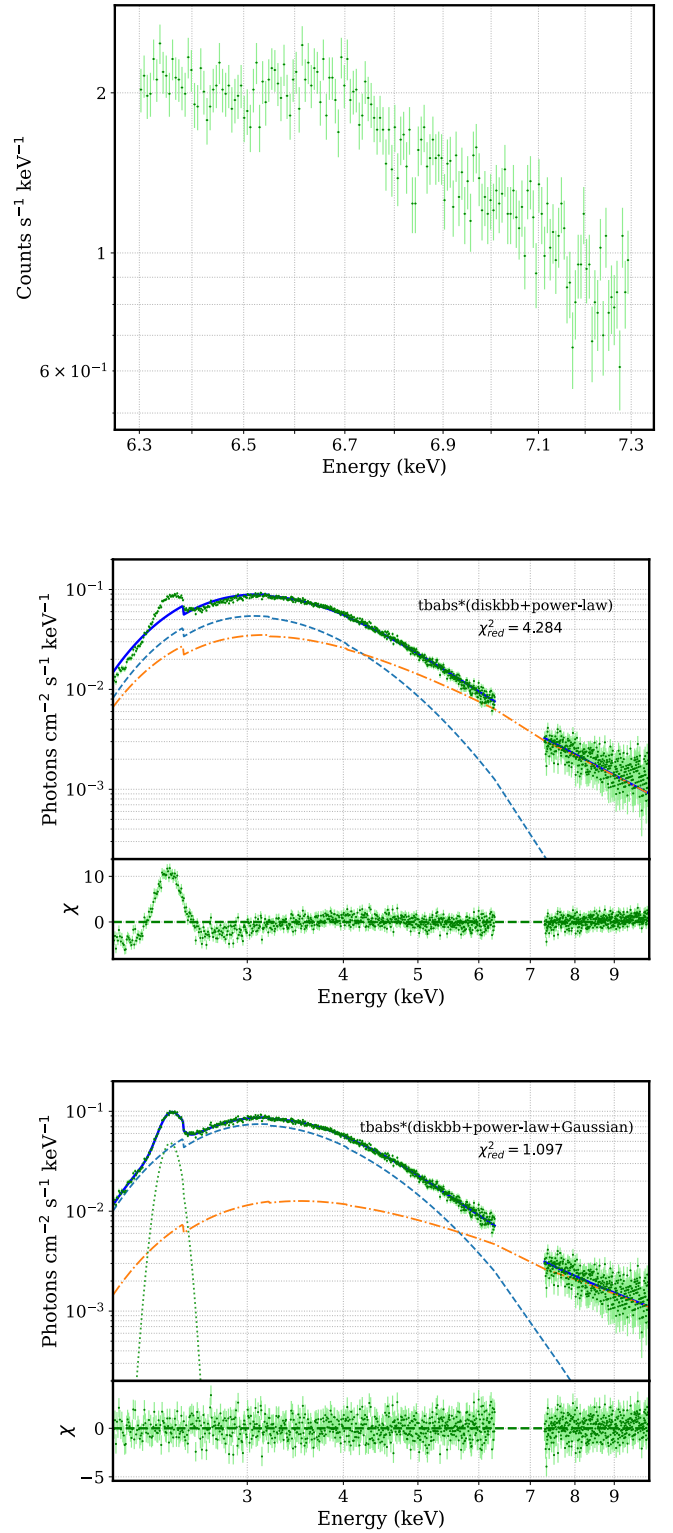


Figure 2. The Xtend spectrum in the range 6.3–7.3 keV is shown in the upper panel. The middle and lower panels represent the fitted continuum in the 2–10 keV energy band, ignoring the 6.3–7.3 keV region.

combination reads as `tbabs*(diskbb + po + ga)` for which $\chi^2_{\text{red}} = 1.09$, as shown in the lower panel of Figure 2.

The similar spectral features have been observed while fitted using other models in the following subsections. The details of the model fitting and parameters are described below.

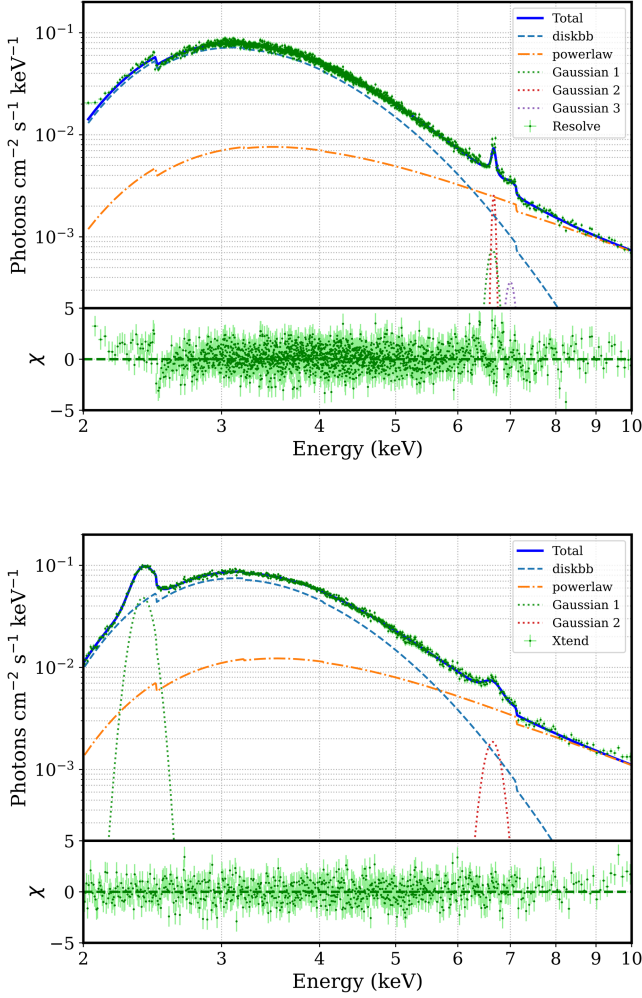


Figure 3. Model-fitted unfolded XRISM spectra for Resolve (top panel) and Xtend (bottom panel) instruments, respectively, by using a combination of diskbb, power-law, and Gaussian models.

3.2. Continuum and Emission Line Modeling

Here, we describe the results and model-fitted parameters from the combined continuum and line emission models.

3.2.1. diskbb and power-law

After finding the best-fitted continuum model, we included the 6.3–7.3 keV energy band in our analysis, which is the main motivation of this work. We found that there is the presence of a triplet line emission in this energy band for the Resolve spectrum. Thus, to get the best fit, we added three *ga* lines, and our best-fitted model combination reads as $\text{tbabs}^*(\text{diskbb} + \text{po} + \text{ga}[3])$ and achieves $\chi^2_{\text{red}} = 1.09$. The best-fitted unfolded spectrum is given in the upper panel of Figure 3.

The spectrum from the Resolve instrument showed the presence of multiple line emissions in the 6.3–7.3 keV energy band. From the spectral fitting, we found that the N_{H} was high with a value of $(16.7 \pm 0.1) \times 10^{22} \text{ cm}^{-2}$. The source is located in a very crowded region near the Galactic center. Due to its close proximity to the Galactic center, the MAXI satellite could not distinctly resolve the source. The inner disk temperature (T_{in}) is $0.62 \pm 0.04 \text{ keV}$. The diskbb model normalization, $\text{Norm}_{\text{diskbb}}$ obtained from the best fit, is 6339 ± 269 . We found that the photon index of the power

Table 1

Values of the Spectrally Fitted Parameters Using *tbabs*, *diskbb*, *power-law*, and Multiple Gaussian Models

(1) Parameters	(2) Resolve	(3) Xtend
N_{H}	16.7 ± 0.1	17.9 ± 0.15
T_{in}	0.62 ± 0.04	0.60 ± 0.05
$\text{Norm}_{\text{diskbb}}$	6339 ± 269	9812 ± 578
Γ	3.2 ± 0.1	3.3 ± 0.1
Norm	1.21 ± 0.27	2.46 ± 0.62
E_{Ga1}	6.64 ± 0.11	2.36 ± 0.12
σ_{Ga1}	0.10 ± 0.04	0.07 ± 0.01
Norm_{Ga1}	$2e - 4 \pm 4e - 5$	0.21 ± 0.01
E_{Ga2}	6.67 ± 0.17	6.64 ± 0.13
σ_{Ga2}	0.03 ± 0.01	0.16 ± 0.02
Norm_{Ga2}	$3e - 4 \pm 4e - 5$	$9e - 4 \pm 8e - 5$
E_{Ga3}	6.99 ± 0.02	...
σ_{Ga3}	0.10 ± 0.04	...
Norm_{Ga3}	$1e - 4 \pm 2e - 5$...
$\chi^2/\text{degrees of freedom}$	6792/6235	1408/1321
Flux	1.05 ± 0.01	1.22 ± 0.12

Note. Column (1) represents the parameters of the phenomenological models used for spectral fitting. Columns (2) and (3) represent the values of those parameters for the Resolve and the Xtend instruments, respectively. The last value of flux is in the units of $10^{-9} \text{ erg cm}^{-2} \text{ s}^{-1}$.

law was very high with a value of $\Gamma \sim 3.2 \pm 0.1$, suggesting that the source is in the soft state during this epoch of the outburst. We find that there was the presence of iron lines at ~ 6.64 , 6.67 , and 6.99 keV , with widths 100 ± 30 , 35 ± 3 , and $100 \pm 40 \text{ eV}$, respectively. All the lines have a normalization value of the order of 10^{-4} . These are possibly the multiple components of the Fe XXV lines; however, they are subject to a detailed line profile study. In column (2) of Table 1, the best-fitted model parameters are listed.

For the Xtend spectrum, as mentioned before, the line features are not resolved properly to identify them as multiple lines. Thus, we only added one *ga* component to the previously achieved best-fitted continuum for Xtend. Thus, our best-fitted model combination reads as $\text{tbabs}^*(\text{diskbb} + \text{po} + \text{ga}[2])$ for which $\chi^2_{\text{red}} = 1.07$. The best-fitted unfolded spectrum is given in the lower panel of Figure 3.

For the Xtend, the line components were not resolved properly and looked like a broad Gaussian component. From this spectral fitting, we also found that the N_{H} was high with a value of $(17.9 \pm 0.1) \times 10^{22} \text{ cm}^{-2}$. The inner disk temperature (T_{in}) is $0.60 \pm 0.05 \text{ keV}$. The diskbb model normalization, $\text{Norm}_{\text{diskbb}}$ obtained from the best-fit is 9812 ± 578 . Here also, the high value of the photon index of the power law $\Gamma \sim 3.3 \pm 0.1$ suggests the presence of the high soft state. We found the presence of an iron line at the line energy of $6.64 \pm 0.01 \text{ keV}$ with a width of $161 \pm 17 \text{ eV}$ and a normalization of the order of $\sim 10^{-3}$. There was the presence of an excess flux at the low energy of $\sim 2.36 \pm 0.02 \text{ keV}$ with a width of $70 \pm 2 \text{ eV}$. However, the normalization of this Gaussian was $\sim 0.21 \pm 0.01$. This can be observed in the lower panel of Figure 3. As mentioned earlier, we speculate it could be from the instrumental effect rather than astrophysical. In column (3) of Table 1, the best-fitted model parameters are listed. We also estimated the line intensity ratio ($I_{6.9}/I_{6.7}$) of the ~ 6.99 to $\sim 6.7 \text{ keV}$ (adding both the lines at 6.64 and 6.67 keV). We found that it is ~ 0.29 , confirming the location

of the source near the Galactic center (M. Nobukawa et al. 2016).

To further estimate the inner disk radius, i.e., the extent of the inner disk, we used the scaling relation, $\text{Norm}_{\text{diskbb}} = (r_{\text{in}}/D_{10})^2 \cos \theta$, where r_{in} , D_{10} , and θ are the inner disk radius (in kilometers), the distance of the source (in units of 10 kpc), and the inclination of the disk (in degrees) to the observer, respectively. However, the abovementioned r_{in} is subject to some uncertainty (T. Shimura & F. Takahara 1995; A. Kubota et al. 1998). The modified inner disk radius is given by $R_{\text{in}} \simeq \kappa^2 \xi r_{\text{in}}$, where κ and ξ are the hardening factor (A. Kubota et al. 1998) and inner boundary correction factor (T. Shimura & F. Takahara 1995), respectively. According to them, these two correction factors have values of 1.7 and 0.41, respectively. Thus, the relation becomes $\text{Norm}_{\text{diskbb}} = (R_{\text{in}}/\kappa^2 \xi D_{10})^2 \cos \theta$. So, the correct inner disk radius (R_{in}) is given as $R_{\text{in}} = (\kappa^2 \xi D_{10}) \sqrt{(\text{Norm}_{\text{diskbb}}/\cos \theta)}$. According to S. Mandel et al. (2025), we also assume a distance estimate of the source as 8 kpc. Since the disk inclination of the source is not constrained, we assume values of $\theta \sim 20^\circ$, 50° , and 80° for low to high inclination. Given these values, the R_{in} comes out to be $\sim\{78, 94, \text{ and } 184\}$, and $\sim\{97, 118, \text{ and } 229\}$ km for Resolve and Xtend instruments, respectively. Considering the innermost stable circular orbit for the inner disk radius of a Schwarzschild black hole as a scale factor, the mass of this source varies from 8 to 25 M_\odot . Due to the consideration of a broad range of inclination, the mass has also appeared in a broad range. Such estimates can provide preliminary information about the black hole mass as a parameter, but not the physical properties of the system.

3.2.2. Kerrbb and Power-Law

We also performed the spectral analysis by using the *kerrbb* (see footnote 13) model (L.-X. Li et al. 2005) by replacing the *diskbb* component. To perform the spectral fitting with this model, we have frozen the distance of the source to 8 kpc (S. Mandel et al. 2025, though not yet confirmed) and also frozen the hardening factor to 1.7. The use of *kerrbb* model can give preliminary information about the intrinsic properties of the BH. Previously, the *kerrbb* model has been used to constrain fundamental properties of black hole systems like spin parameter during high soft state (M. Pahari et al. 2018).

For Resolve, the best-fitted model combination reads as $\text{tbabs}^*(\text{kerrbb} + \text{po} + \text{ga}[3])$ with $\chi^2_{\text{red}} \sim 1.09$. The best-fitted unfolded spectrum is shown in the upper panel of Figure 4. For Xtend, the best-fitted model combination reads as $\text{tbabs}^*(\text{kerrbb} + \text{po} + \text{ga}[2])$, with a $\chi^2_{\text{red}} \sim 1.07$. The best-fitted unfolded spectrum is shown in the lower panel of Figure 4.

From this model fitting, we found that the disk has a low inclination of $\sim 19^\circ$ – 24° and a moderate BH spin of ~ 0.63 – 0.70 . This low inclination suggests that the inner disk might be at a distance of ~ 75 – 100 km from the central object, obtained from the previous relation. The *kerrbb* model fit determines the mass to be 8.5 – $10.1 M_\odot$. The little disagreement between the two models in M_{BH} estimation appears due to the choice of disk inclination. When performing the *kerrbb* fitting, we kept the inclination as a free parameter and found a return value in the 19° – 24° range, whereas for the *diskbb* case, we assumed inclination values of 20° , 50° , and 80° . If we consider the low inclination of $<25^\circ$ in *diskbb*

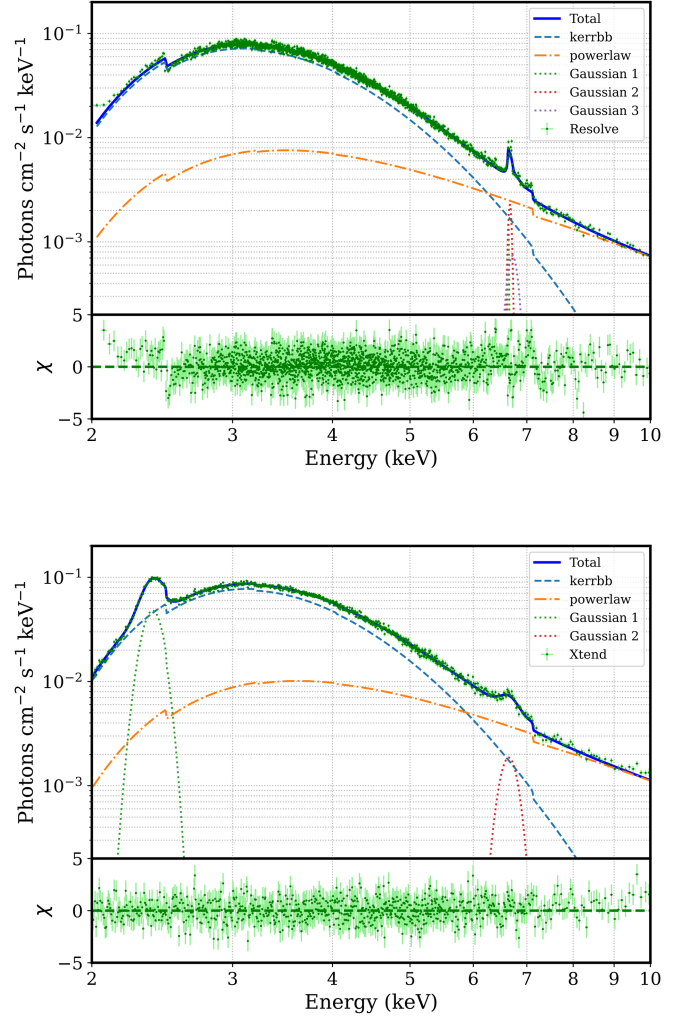


Figure 4. Model-fitted unfolded XRISM spectra for Resolve (top panel) and Xtend (bottom panel) instruments, respectively, by using a combination of *kerrbb*, power-law, and Gaussian models.

estimations, both models provide a similar black hole mass. Since both models are phenomenological, to better constrain the parameter, data fitting using a more realistic model is required. Those estimations can be further verified and confirmed using the dynamical study of the source. Nonetheless, the present estimations further suggest that the object is a black hole and not a neutron star. Considering this mass, agrees that the inner boundary of the disk has moved inside the $6r_g$ distance from the object, which makes it suitable for iron line emission ($6r_g$ to $30r_g$). The results of this model fitting are given in Table 2.

3.2.3. JeTCAF

In addition to these models, we have also implemented the physically motivated accretion-ejection-based JeTCAF model by replacing the PL model to estimate the accretion-ejection parameters and the mass of the BH. Since JeTCAF has both hot (corona) and cold (disk) flow components, it can be fitted to any spectral states, whether a jet is present or not. Depending on the spectral state, model parameters can be constrained. As the source is in the soft state, that will be imprinted in the jet parameters as well, which can be further verified using this model. There are six parameters in this

Table 2Values of the Spectrally Fitted Parameters Using `tbabs`, `kerrbb`, power-law, and Multiple Gaussian Models

(1) Parameters	(2) Resolve	(3) Xtend
N_H	17.0 ± 0.2	18.1 ± 0.7
spin (a)	0.68 ± 0.02	0.65 ± 0.02
inclination (i)	19.8 ± 0.3	23.4 ± 0.3
Mass (M_{BH})	8.8 ± 0.3	9.6 ± 0.5
Mdd	0.86 ± 0.03	0.87 ± 0.04
Norm _{kerrbb}	1.7 ± 0.2	2.27 ± 0.3
Γ	3.2 ± 0.2	3.1 ± 0.6
Norm	1.25 ± 0.13	1.62 ± 0.25
E_{Ga1}	6.64 ± 0.14	2.36 ± 0.11
σ_{Ga1}	0.01 ± 0.00	0.07 ± 0.01
Norm _{Ga1}	$8e - 5 \pm 2e - 5$	0.22 ± 0.02
E_{Ga2}	6.67 ± 0.32	6.64 ± 0.14
σ_{Ga2}	0.03 ± 0.01	0.16 ± 0.02
Norm _{Ga2}	$2e - 4 \pm 4e - 5$	$9e - 4 \pm 8e - 5$
E_{Ga3}	6.72 ± 0.03	...
σ_{Ga3}	0.10 ± 0.01	...
Norm _{Ga3}	$2e - 4 \pm 4e - 5$...
$\chi^2/\text{degrees of freedom}$	6801/6232	1406/1318
Flux	1.05 ± 0.02	1.22 ± 0.01

Note. Column (1) represents the parameters of the models used for spectral fitting. Columns (2) and (3) represent the values of those parameters for the Resolve and the Xtend instruments, respectively. The last value of flux is in the units of $10^{-9} \text{ erg cm}^{-2} \text{ s}^{-1}$.

model, including the mass of the BH if it is not dynamically measured. The parameters are: (i) mass of the BH (M_{BH} in solar mass M_\odot units) (ii) cold Keplerian disk accretion rate (\dot{m}_d), (iii) hot sub-Keplerian halo accretion rate (\dot{m}_h) (both rates are in Eddington rate \dot{M}_{Edd}), (iv) size of the corona; shock location (X_s in gravitational radius $r_g = GM_{BH}/c^2$), (v) density jump across the shock; compression ratio ($R = \rho_+/\rho_-$, where ρ_+ and ρ_- represent the densities in the postshock and preshock flows), and (vi) outflow collimation factor (f_{col}), the ratio of the solid angle subtended by the outflow to the inflow (Θ_o/Θ_i). Since the model has BH mass as a free parameter, one can successfully determine its value from the spectral modeling (see D. Debnath et al. 2014; A. A. Molla et al. 2017; S. Mondal et al. 2024).

The model combination reads in XSPEC as: `tbabs (JeTCAF + ga[7])` for Resolve. The best-fitted unfolded spectrum could be seen in the upper panel of Figure 5. Given the above model combinations, the Resolve spectrum is best-fitted with $\chi^2_{red} = 1.3$ using the JeTCAF model for the parameters $M_{BH} = 5.7 \pm 0.8 M_\odot$, $\dot{m}_d = 2.76 \pm 0.21$, $\dot{m}_h = 0.25 \pm 0.06$, $X_s < 12$, $R = 6.52 \pm 1.37$, and $f_{col} = 0.12 \pm 0.03$. The high disk mass accretion compared to the hot sub-Keplerian component infers the soft spectral state. The Keplerian disk moved much closer to the BH $< 12 r_g$ (pegged at the lower bound of the parameter space), which is also associated with the effect of cooling due to the high disk accretion rate that cooled the hot corona. Such phenomena have also been observed for other LMBHs studied using the TCAF model (S. Mondal et al. 2014, 2017; K. Chatterjee et al. 2021, 2023). The high value of R and low value of f_{col} refer to the low mass outflow (see S. K. Chakrabarti 1999; S. Mondal & S. K. Chakrabarti 2021) as expected in the soft state. Similar to other models, N_H obtained from the fit is also high

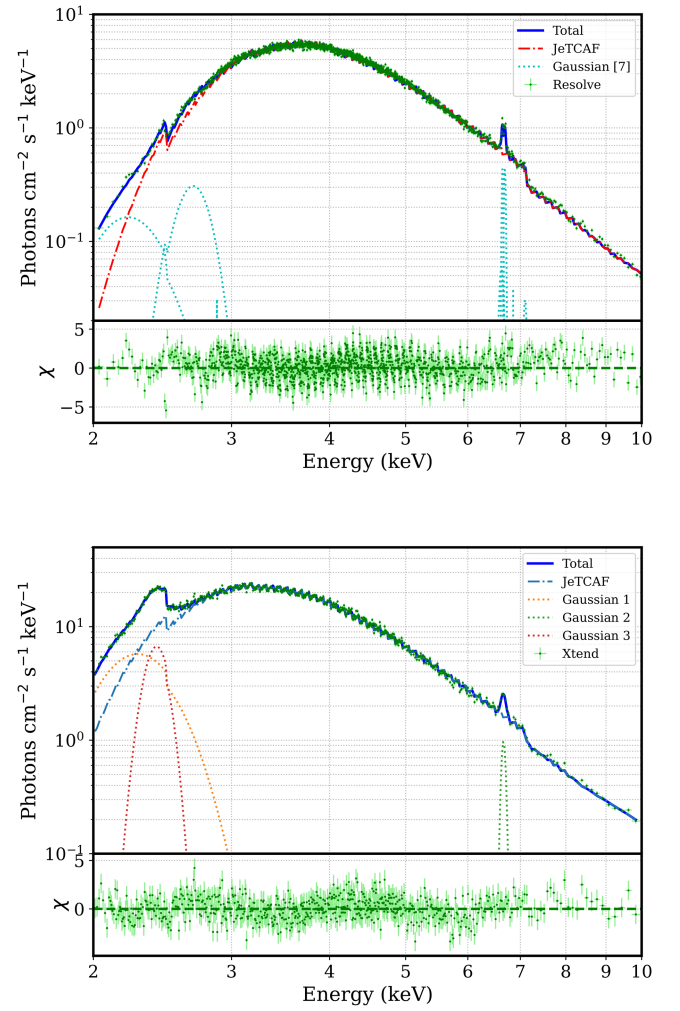


Figure 5. Best-fitted JeTCAF model fitted spectra in the 2–10 keV energy band are shown. The top and bottom panels represent the Resolve and Xtend instruments, respectively. The bottom windows of each panel show the residuals of the fits.

$(37.2 \pm 0.2) \times 10^{22} \text{ cm}^{-2}$. Since there are multiple Fe K lines, we have frozen them to their peak energies at 6.62, 6.64, 6.69, 6.85, and 7.1 keV and let their width vary. The best-fitted line width σ for all Fe K lines is $< 0.03 \text{ keV}$.

For Xtend, the best-fitted model combination reads as `tbabs* (JeTCAF + ga[3])`. The Xtend data equally fit well for a marginal change within error in the JeTCAF model parameter as in Resolve with $\chi^2_{red} = 1.2$. The N_H value required for the Xtend data fitting is $(24.8 \pm 0.1) \times 10^{22} \text{ cm}^{-2}$. The best-fitted model spectra are shown in Figure 5.

The above model fittings help summarize the estimate of the mass of the BH. The `diskbb` model fits determined the mass in the range $8\text{--}25 M_\odot$ for different values of the disk inclination angle, which is later better constrained by using the `kerrbb` model fit. The estimated mass of the BH turns out to be $\approx 8\text{--}10 M_\odot$ from the above two models. From the JeTCAF model fits, the mass of the BH comes out to be $\approx 5.7 \pm 0.8 M_\odot$. Combining these three estimates, the most probable mass of the central compact object becomes $7.9 \pm 2.2 M_\odot$.

The estimation of M_{BH} can be done using a more direct method from the dynamics of the stars orbiting the BH, which requires very high-resolution optical telescopes. So far, only a handful of sources (less than one-third of total discovered black

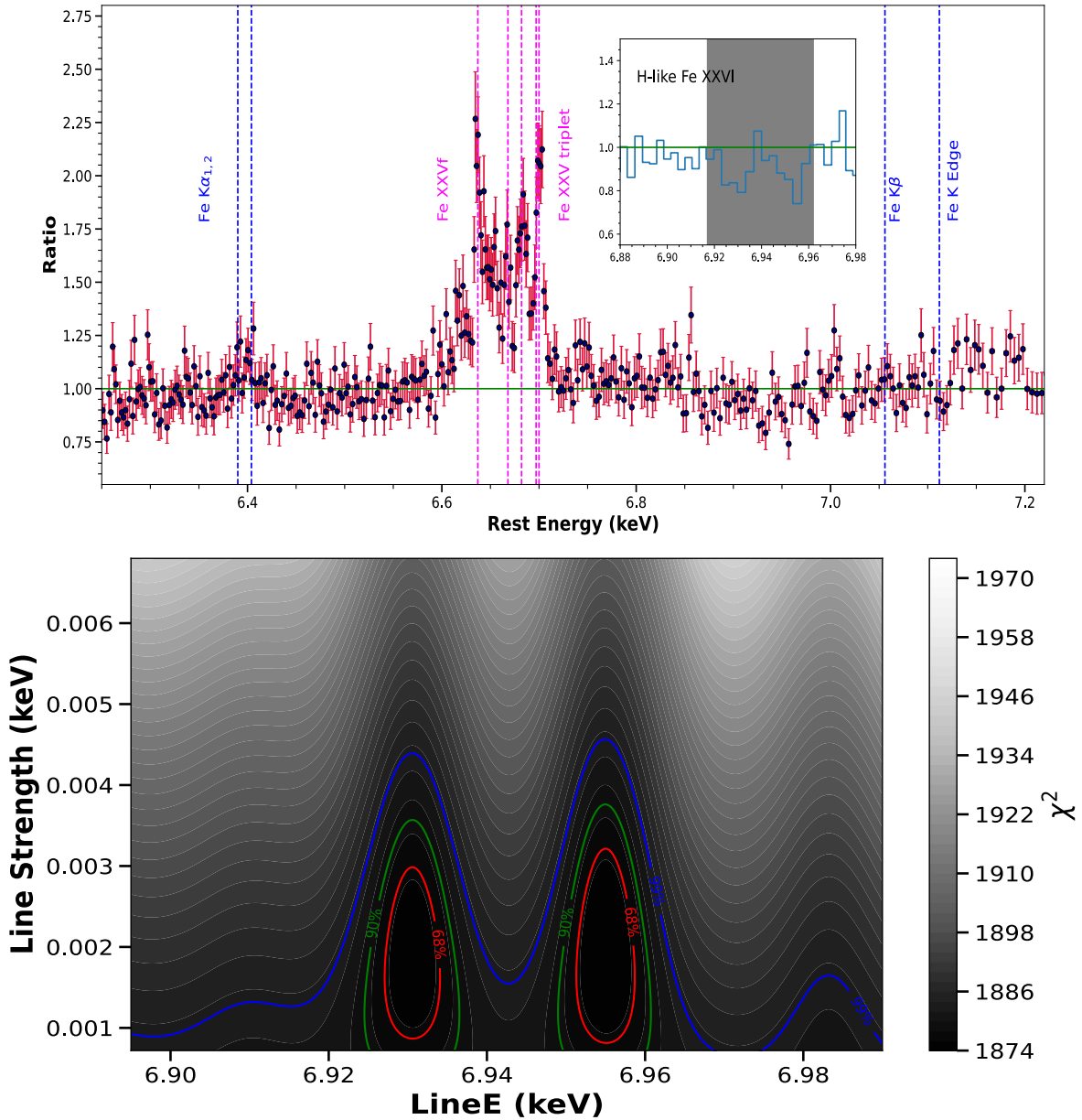


Figure 6. Top panel: residuals from continuum-subtracted 6–7 keV Resolve spectrum showing a wealth of complex Fe K lines marked using vertical dashed lines. The He-like Fe XXV emission complex dominates the residuals, showing a mix of forbidden and recombination transitions. An inset plot shows a zoomed-in view of 6.9 keV, capturing weak H-like Fe XXVI absorption line features. Bottom panel: *steppar* results for absorption line energy and normalization after scanning a narrow Gaussian absorption to the continuum model. The red, green, and blue contours correspond to 68%, 90%, and 99% confidence levels.

hole candidates (BHCs); see BlackCat¹⁸ are dynamically confirmed due to a lack of resolution (J. M. Corral-Santana et al. 2016). The mass of the BH is one of the fundamental quantities that is required to further study the system in greater detail. Therefore, we have estimated its value using the indirect method by modeling the X-ray spectra. Among the different methods discussed above, the TCAF model or its variant (JeTCAF) has the potential to robustly measure the BH mass (A. A. Molla et al. 2016, 2017), which has further produced consistent results in optical (for MAXI J1659–152; J. M. Corral-Santana et al. 2018). Additionally, a detailed and fully general relativistic treatment of mass estimation has also agreed with our mass estimation from spectral modeling (e.g.,

for H 1743–322; A. A. Tursunov & M. Kološ 2018). In the same line, we believe that the mass estimated in this work for the present source may remain valid within error and can be verified further in the future using optical studies.

From all the modeling, we got very high values of the hydrogen column density (N_{H}). This may be because the source is situated in the Galactic center. The overly dense gas cloud (XRISM Collaboration et al. 2025) in the Galactic center may have blocked radiation, resulting in a high N_{H} .

3.3. Photoionization Modeling (*photemis*)

The source MAXI J1744–294 showed complex Fe emission features between 6 and 7 keV in the Resolve spectrum. The left panel of Figure 6 shows the continuum-subtracted 6–7 keV

¹⁸ <https://www.astro.puc.cl/BlackCAT/>

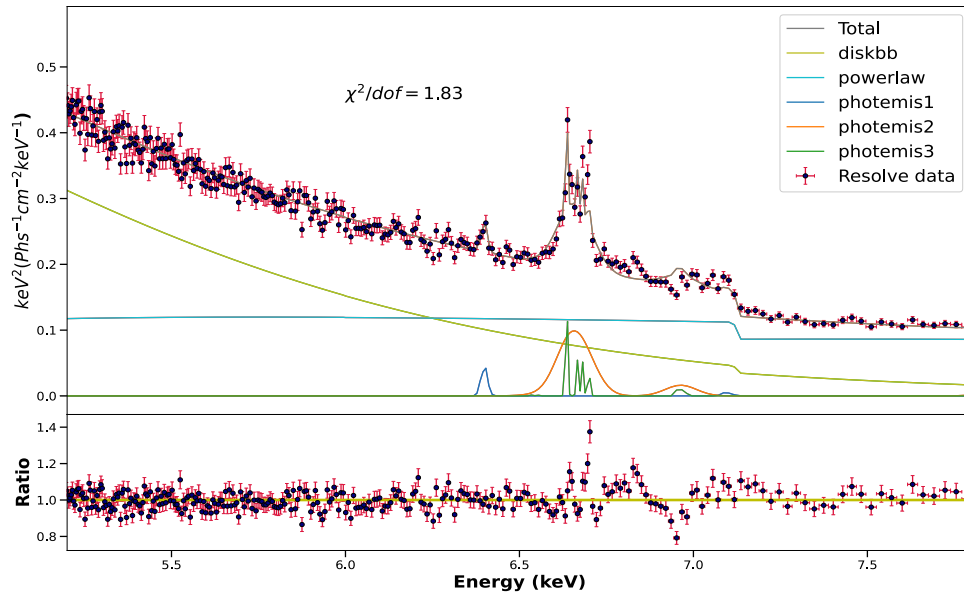


Figure 7. Best-fitted `photemis` model fitted to the 5–8 keV Resolve spectrum is shown. The top and bottom panels represent the decomposition of model components and residuals, respectively.

Table 3
Best-fit Parameters of the Photoionization Model

Component	$\log \xi$	v_{turb} (km s^{-1})	Norm_{pht}
photemis #1	1.55 ± 0.05	153.29 ± 54.56	1561.36 ± 293.49
photemis #2	3.17 ± 0.15	2513.30 ± 206.48	522.95 ± 38.24
photemis #3	3.15 ± 0.05	$= \#1$	94.13 ± 18.48

Resolve spectrum. We clearly detected a weak Fe $K\alpha$ doublet ($K\alpha_{1,2}$) along with Fe $K\beta$ and $K\alpha$ edge. Strong He α -like complex Fe XXV (forbidden and triplet) emission lines between 6.6 and 6.7 keV were detected. As shown in the inset, weak absorption features corresponding to Fe XXVI were detected. We added a narrow absorption component `gabs` to the continuum model and scanned the 6.8–7 keV range using `steppar` command. While the width was frozen to 5 eV, the line energy centroid and line strength were varied for 1000 x 1000 iterations. The right panel of Figure 6 shows a weak, but significant detection of Fe XXVI absorption feature, which is redshifted to ~ 6.94 keV from the rest frame by $z = -0.0043$. So far, we have used phenomenological multiple Gaussian components to fit different Fe K line transitions. However, to produce the line profiles, a realistic emission model is favorable. Therefore, we adopted the publicly available `photemis` model, derived from the `XSTAR` photoionization code (T. Kallman & M. Bautista 2001). It consists of analytically computed spectra produced by recombined and collisionally ionized plasma.

While fitting the Resolve data between 5 and 8 keV, we kept the line of sight N_{H} and T_{in} fixed to prior obtained values of $16.7 \times 10^{22} \text{ cm}^{-2}$ and 0.62 keV, as they cannot be constrained in the narrowband spectrum. The spectra were rebinned to a minimum of 500 counts per bin. We used the standard precalculated ion population of `xstar`, setting all abundances to zero except for iron, which was frozen to 1. The remaining free parameters were ionization parameter ($\log \xi$), turbulent velocity (v_{turb}), and normalization (Norm_{pht}). We found that a combination of three `photemis` components was able to

satisfactorily describe the spectral line features between 6 and 7 keV. The best-fitted model decomposition, along with residuals, is shown in Figure 7. The best fit values are presented in Table 3.

The photoionized emission was modeled by a low-ionization component ($\log \xi \sim 1.56$) that accounts for Fe $K\alpha$ emission around 6.40 keV and two highly ionized components ($\log \xi \sim 3$) that wholly reproduce the Fe XXV emission complex. We tied the turbulent velocity of two narrow components (`photemis` #1 and #3) while keeping the broad component (`photemis` #2) free during the fit. Our best-fitted results indicated that the Fe XXV complex originates from two comparably ionized plasmas of $\log \xi = 3.15$ and 3.17, however, showing very distinct velocity widths. The broad component with $v_{\text{turb}} = 2513 \text{ km s}^{-1}$ is most likely produced from extremely hot gas located close to the inner edge of the accretion disk. The lines are broadened under the effect of Keplerian motion of the accretion disk as it extends close to the black hole during the soft spectral state. On the other hand, the narrow component with $v_{\text{turb}} = 153 \text{ km s}^{-1}$ is probably the scattered emission from nearby gas that has been strongly photoionized by hard X-ray radiation. Another narrow, low-ionized component ($\log \xi \sim 1.6$) fits the weak Fe $K\alpha$ line, which originates further away from the accreting source, in a much cooler and less dense region.

Therefore, our analysis of multiple Fe K emission lines in the soft state in this source reveals contributions from neutral, He-like, and H-like iron. This is unusual compared to the traditional picture of a single, uniform reflection component for X-ray binaries (XRBs), indicating instead a stratified reprocessing medium spanning the accretion disk and possibly disk winds in the soft state. The distinct line components allow separate constraints on ionization rates, velocity broadening, and possibly the geometry of the medium (subject to detailed modeling), providing further detail on the ionization gradient of the reflector. Moreover, these results suggest a possible coupling between inflow and outflow in the soft state of the accreting systems, making the source more interesting to

further study with possible potential applications to other transients.

Since this source is located close to the Galactic center, the emission line complex is expected to be contaminated by X-ray diffuse emission from stellar populations in the Galactic bulge and unresolved, accreting magnetic cataclysmic variables (M. Revnivtsev et al. 2009; K. Anastasopoulou et al. 2023). This could potentially explain the residuals around ~ 6.7 and 6.8 keV. The persistent narrow emission feature around 6.85 keV does not correspond to any recognized atomic transition. We speculate that this could be due to a redshifted Fe XXVI transition originating from ionized, outflowing winds. We also noticed clear, broad residuals around 7 keV as well, which, most likely, is due to the blended emission from Fe XXVI Ly α and Fe K β lines, requiring sophisticated handling of photoionization models, which is beyond the scope of this work.

Presence of a significant and strong Fe absorption feature in the X-ray spectra is often interpreted as characteristic of high inclination X-ray binaries (L. Boirin & A. N. Parmar 2003; L. Boirin et al. 2004). Despite the high spectral resolution and high signal-to-noise ratio in 6 – 7 keV, the detection of a weak absorption feature (Figures 6 and 7) supports the low inclination, nondipping nature of the source. This is further supported by our estimation of low inclination (19° – 24°) from continuum disk modeling using `kerrbb` (see Table 2). Interestingly, the detection of a mild redshifting in this absorption feature could be a signature of failed winds, similar to that observed in BH transient 4U 1630-472 (J. M. Miller et al. 2025). At a few percent of Eddington luminosity, the source MAXIJ1744–294 could be hosting such winds that were launched vertically from the disk and became bound to the system. Follow-up monitoring, especially during the quiescent and outburst phases, can provide more insights into the gaseous kinematics of this system.

4. Conclusions

We have studied the spectral properties of the BHC MAXIJ1744–294 after its very first detection in 2025. Using publicly available archived XRISM data on 2025 March 3 (MJD 60737), we have studied the spectrum of the source using both the instruments of this satellite, namely, Resolve and Xtend. The spectacular spectral resolution of the XRISM satellite, especially the Resolve, helps us find the existence of multiple iron line profiles in the spectra. In Xtend, we also found the existence of an iron line. To take care of the continuum emission, we have used various combinations of phenomenological and physical models (`diskbb`, `kerbb`, `power-law`, `JeTCAF`, and `photemis`). To take care of the line emissions, we have used multiple lines in the form of the Gaussian model with continuum models. Along with these, we have used an interstellar absorption model, `tbabs`. We have achieved the best fits with these models. We have also implemented the photoionization modeling in the same spectra using the `photemis` analytic models implemented in `XSPEC`. This is one of the detailed studies of both continuum and line profiles of a low-mass X-ray binary in recent times. From our model-fitted results, we conclude that:

1. The system is situated in a crowded region close to the Galactic center, supported by the ratios of the iron lines, resulting in a high hydrogen column density. The data

could be well explained by models with disk inclination of $i \sim 19^\circ$ – 24° , black hole spin of $a \sim 0.63$ – 0.70 , and a mass of $M_\odot \sim 7.9 \pm 2.2 M_\odot$.

2. From the values of the photon index, inner disk temperature, inner disk radius, and accretion rates, we conclude that the source was in the soft spectral state during this time of outburst activity.
3. High-resolution XRISM spectroscopy has revealed, for the first time, complex iron line features in this source, corresponding to distinct components of Fe XXV emission along with Fe XXVI absorption features.
4. These Fe XXV line complexes arise from two highly ionized plasmas ($\log \xi \sim 3$) with distinct turbulent velocities—one broad ($v_{\text{turb}} \approx 2513 \text{ km s}^{-1}$) from hot gas at the inner accretion disk, and one narrow ($v_{\text{turb}} \approx 153 \text{ km s}^{-1}$) scattered by nearby photoionized gas. A separate low-ionization component ($\log \xi \sim 1.6$) accounts for the weak, narrow Fe K α fluorescent line from cooler, distant regions. These results offer new insight into the reprocessing of continuum in stratified media, either in the accretion disk or winds, or both, for XRBs in the soft state.

Acknowledgments








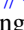


We thank the referee for making valuable comments and suggestions. We thank Michael Loewenstein of the University of Maryland, College Park, USA, for his assistance during the data reduction. K.C., C.B.S., B.K., and X.-W.L. acknowledge support from the “Science & Technology Champion Project” (202005AB160002) and from two “Team Projects”—the “Top Team” (202305AT350002) and the “Innovation Team” (202105AE160021), all funded by the “Yunnan Revitalization Talent Support Program.” They also acknowledge the support from the “Key Laboratory of Survey Science of Yunnan Province” with project No. 202449CE340002. S.M. acknowledges the Ramanujan Fellowship (# RJF/2020/000113) by SERB/ANRF-DST, Govt. of India, for this research. B.P. acknowledges collective support from Narodowe Centrum Nauki (NCN) grants 2021/41/B/ST9/04110 and 2018/31/G/ST9/03224 for this research. C.B.S. is also supported by the National Natural Science Foundation of China under grant No. 12073021. B.K. also acknowledges the support from the ‘Special Project for High-End Foreign Experts, Xingdian Funding from Yunnan Province, and the National Key Research and Development Program of China (2024YFA1611603). H.-K.C. acknowledges support from the NSTC project (grant No. 114-2112-M-007-042) of NTHU.

Data Availability

This work has made use of publicly archived data from the XRISM satellite, which is a mission of the Japan Aerospace Exploration Agency in partnership with NASA and ESA. This work has also made use of software from the HEASARC, which is developed and monitored by the Astrophysics Science Division at NASA/GSFC and the High Energy Astrophysics Division of the Smithsonian Astrophysical Observatory.

Software: HEASOFT (version: 6.35.1), XSPEC (version: 12.15.0; K. A. Arnaud 1996), Matplotlib (version: 3.6.1; J. D. Hunter 2007), XSTAR (version: 2.58; T. Kallman & M. Bautista 2001), XRISM Pipelines with `caldb` (version: 20250315 for Resolve; version: 20241115 for Xtend and GEN).

ORCID iDs

Kaushik Chatterjee  <https://orcid.org/0000-0002-6252-3750>
 Santanu Mondal  <https://orcid.org/0000-0003-0793-6066>
 Biswaraj Palit  <https://orcid.org/0000-0002-4533-3170>
 Chandra B. Singh  <https://orcid.org/0000-0002-7782-5719>
 Sujoy Kumar Nath  <https://orcid.org/0000-0002-6640-0301>
 Mayukh Pahari  <https://orcid.org/0000-0002-5900-9785>
 Brajesh Kumar  <https://orcid.org/0000-0001-7225-2475>
 Wei Wang  <https://orcid.org/0000-0003-3901-8403>
 Hsiang-Kuang Chang  <https://orcid.org/0000-0002-5617-3117>
 Xiaowei Liu  <https://orcid.org/0000-0003-1295-2909>

References

- Anastasopoulou, K., Ponti, G., Sormani, M. C., et al. 2023, *A&A*, **671**, A55
 Arnaud, K. A. 1996, in ASP Conf. Ser. 101, *Astronomical Data Analysis Software and Systems V*, ed. G. H. Jacoby & J. Barnes (San Francisco, CA: ASP), 17
 Asai, K., Dotani, T., Nagase, F., & Mitsuda, K. 2000, *ApJS*, **131**, 571
 Belloni, T., Psaltis, D., & van der Klis, M. 2002, *ApJ*, **572**, 392
 Boirin, L., & Parmar, A. N. 2003, *A&A*, **407**, 1079
 Boirin, L., Parmar, A. N., Barret, D., Paltani, S., & Grindlay, J. E. 2004, *A&A*, **418**, 1061
 Brenneman, L. W., & Reynolds, C. S. 2006, *ApJ*, **652**, 1028
 Casella, P., Belloni, T., & Stella, L. 2005, *ApJ*, **629**, 403
 Chakrabarti, S., & Titarchuk, L. G. 1995, *ApJ*, **455**, 623
 Chakrabarti, S. K. 1999, *A&A*, **351**, 185
 Chakrabarti, S. K., Debnath, D., Nandi, A., & Pal, P. S. 2008, *A&A*, **489**, L41
 Chatterjee, K., Debnath, D., Chatterjee, D., Jana, A., & Chakrabarti, S. K. 2020, *MNRAS*, **493**, 2452
 Chatterjee, K., Debnath, D., Chatterjee, D., et al. 2021, *Ap&SS*, **366**, 63
 Chatterjee, K., Debnath, D., Nath, S. K., & Chang, H.-K. 2023, *ApJ*, **956**, 55
 Chatterjee, K., Mondal, S., Singh, C. B., & Sugizaki, M. 2024, *ApJ*, **977**, 148
 Chatterjee, K., Suribhatla, S. P., Mondal, S., & Singh, C. B. 2025, *ApJ*, **987**, 44
 Corbel, S., & Fender, R. P. 2002, *ApJL*, **573**, L35
 Corral-Santana, J. M., Casares, J., Muñoz-Darias, T., et al. 2016, *A&A*, **587**, A61
 Corral-Santana, J. M., Torres, M. A. P., Shahbaz, T., et al. 2018, *MNRAS*, **475**, 1036
 Debnath, D., Chakrabarti, S. K., & Mondal, S. 2014, *MNRAS*, **440**, L121
 Dhawan, V., Mirabel, I. F., & Rodríguez, L. F. 2000, *ApJ*, **543**, 373
 Done, C., Gierliński, M., & Kubota, A. 2007, *A&ARv*, **15**, 1
 Fabian, A. C., Rees, M. J., Stella, L., & White, N. E. 1989, *MNRAS*, **238**, 729
 García, J., & Kallman, T. R. 2010, *ApJ*, **718**, 695
 George, I. M., & Fabian, A. C. 1991, *MNRAS*, **249**, 352
 Haardt, F., & Maraschi, L. 1993, *ApJ*, **413**, 507
 Heinke, C. O., Nakajima, M., Kudo, Y., et al. 2025, *ATel*, **17010**, 1
 Hunter, J. D. 2007, *CSE*, **9**, 90
 Iwasawa, K., Fabian, A. C., Reynolds, C. S., et al. 1996, *MNRAS*, **282**, 1038
 Jaisawal, G. K., Steiner, J. F., Strohmayer, T. E., et al. 2025, *ATel*, **17040**, 1
 Kallman, T., & Bautista, M. 2001, *ApJS*, **133**, 221
 Kubota, A., Tanaka, Y., Makishima, K., et al. 1998, *PASJ*, **50**, 667
 Kudo, Y., Negoro, H., Nakajima, M., et al. 2025, *ATel*, **16975**, 1
 Li, L.-X., Zimmerman, E. R., Narayan, R., & McClintock, J. E. 2005, *ApJS*, **157**, 335
 Majumder, S., Kushwaha, A., Singh, S., et al. 2025, arXiv:2506.03774
 Mandel, S., Mori, K., Hailey, C., et al. 2025, *ATel*, **17063**, 1
 Marinucci, A., Matt, G., Miniutti, G., et al. 2014, *ApJ*, **787**, 83
 Marra, L., Mikušincová, R., Vincentelli, F. M., et al. 2025, arXiv:2506.17050
 Matsuoka, M., Kawasaki, K., Ueno, S., et al. 2009, *PASJ*, **61**, 999
 Miller, J. M., Mizumoto, M., Shidatsu, M., et al. 2025, *ApJL*, **988**, L28
 Molla, A. A., Chakrabarti, S. K., Debnath, D., & Mondal, S. 2017, *ApJ*, **834**, 88
 Molla, A. A., Debnath, D., Chakrabarti, S. K., Mondal, S., & Jana, A. 2016, *MNRAS*, **460**, 3163
 Mondal, S., Adhikari, T. P., & Singh, C. B. 2021, *MNRAS*, **505**, 1071
 Mondal, S., & Chakrabarti, S. K. 2021, *ApJ*, **920**, 41
 Mondal, S., Chakrabarti, S. K., Nagarkoti, S., & Arévalo, P. 2017, *ApJ*, **850**, 47
 Mondal, S., Debnath, D., & Chakrabarti, S. K. 2014, *ApJ*, **786**, 4
 Mondal, S., Suribhatla, S. P., Chatterjee, K., Singh, C. B., & Chatterjee, R. 2024, *ApJ*, **975**, 257
 Motta, S., Muñoz-Darias, T., Casella, P., Belloni, T., & Homan, J. 2011, *MNRAS*, **418**, 2292
 Nakajima, M., Negoro, H., Kudo, Y., et al. 2025, *ATel*, **16983**, 1
 Nobukawa, M., Uchiyama, H., Nobukawa, K. K., Yamauchi, S., & Koyama, K. 2016, *ApJ*, **833**, 268
 Pahari, M., Bhattacharyya, S., Rao, A. R., et al. 2018, *ApJ*, **867**, 86
 Pozdnyakov, L. A., Sobol, I. M., & Syunyaev, R. A. 1983, *ASPRv*, **2**, 189
 Remillard, R. A., & McClintock, J. E. 2006, *ARA&A*, **44**, 49
 Revnivtsev, M., Sazonov, S., Churazov, E., et al. 2009, *Natur*, **458**, 1142
 Ross, R. R., & Fabian, A. C. 2005, *MNRAS*, **358**, 211
 Shimura, T., & Takahara, F. 1995, *ApJ*, **445**, 780
 Sunyaev, R. A., & Titarchuk, L. G. 1980, *A&A*, **86**, 121
 Tashiro, M., Maejima, H., Toda, K., et al. 2021, *Proc. SPIE*, **11444**, 1144422
 Tetarenko, B. E., Sivakoff, G. R., Heinke, C. O., & Gladstone, J. C. 2016, *ApJS*, **222**, 15
 Titarchuk, L., & Shrader, C. 2005, *ApJ*, **623**, 362
 Tursunov, A. A., & Kološ, M. 2018, *PAN*, **81**, 279
 Watanabe, S., Aoyama, A., Takeda, T., et al. 2025, *ATel*, **17009**, 1
 XRISM Collaboration, Audard, M., Awaki, H., et al. 2025, *PASJ*, **77**, L1